

## Comparison of optically-derived spectral densities and microwave cross sections in a wind-wave tank

Mary Ruth Keller

Naval Research Laboratory, Washington, DC

Bruce L. Gotwols

Applied Physics Laboratory, The Johns Hopkins University, Laurel, Maryland

William J. Plant and William C. Keller

Applied Physics Laboratory, University of Washington, Seattle

**Abstract.** The most popular model of microwave backscatter from rough water surfaces at mid-incidence angles ( $20^\circ < \theta_i < 70^\circ$ ) is composite surface theory. This theory holds that the backscattered return is directly proportional to the spectral density of centimetric, Bragg-resonant water waves which are tilted and advected by longer waves. A stringent test of this theory is to measure, independently and from the same surface area, the normalized microwave cross section ( $\sigma_0$ ) and the Bragg wave spectral density, and compare them using the theory. In this paper, we use a calibrated optical slope imaging system in a wind-wave tank to measure the two-dimensional wavenumber spectrum of short waves. From these spectra, we calculate both the pure Bragg scattering  $\sigma_0$  which neglects longwave effects and the more complex composite surface  $\sigma_0$ . The results are compared with  $\sigma_0$  obtained from backscatter measurements at *X* band (10 GHz) and *K<sub>a</sub>* band (35 GHz) made between  $28^\circ$  and  $68^\circ$  incidence angle. We find that composite surface theory generally shows better agreement with experiment at both frequencies than pure Bragg scattering theory. The agreement seems best for friction velocities above  $40 \text{ cm s}^{-1}$ . For all friction velocities up to  $70 \text{ cm s}^{-1}$ , however, composite surface theory somewhat underpredicts the actual  $\sigma_0$  in a majority of the cases. This is especially true for horizontal polarization at large incidence angles. We conclude that while composite surface theory accounts for much of the backscatter at both frequencies in the incidence angle range we examined, the discrepancy between the predicted and measured cross sections is sufficiently large that contributions from other scattering processes cannot be ruled out.

### Introduction

The last two decades have seen a remarkable growth in the number of researchers attempting to use microwave techniques to obtain oceanographic data. An important early milestone in the interpretation of oceanographic microwave data was the discovery by *Wright* [1966] of a relation between the microwave backscatter and the height of (infinitesimal) water waves. This phenomenon, commonly called Bragg scattering, is applicable at mid-incidence angles, and has been shown to be equivalent to the perturbation scattering solution of *Rice* [1951]. Taken by itself, Bragg scattering theory cannot be applied at centimeter wavelengths, since the condi-

tion that the wave height be small compared to the microwave wavelength is strongly violated for all but the lowest wind conditions. However, *Wright* [1968] and *Bass et al.* [1968a,b] independently proposed a solution to this impasse in the so-called composite or two-scale model. Here the scattering surface is heuristically broken up into long wavelength components at least several times the Bragg wavelength, and short wave components on the order of the Bragg wavelength. The scattering is treated as if it is simple Bragg scattering from small waves riding on the large-scale waves. The resultant cross section is computed as an integral of the Bragg scattering cross section times the probability density of long wave slope. See *Plant* [1990] for a review.

Techniques for validating microwave scattering models at mid-incidence can be placed in three categories: (1) dependence of the cross section on incidence angle, (2) functional form of the Doppler spectrum, and (3) ab-

Copyright 1995 by the American Geophysical Union.

Paper number 95JC00688.  
0148-0227/95/95JC-00688\$05.00

solute cross-section measurements. The dependence of the cross-section polarization ratio on incidence angle for infinitesimal waves generated in a wave tank was seen by *Wright* [1966] as evidence for the correctness of Bragg scattering. However, under open sea conditions, *Wright* [1968] found the incidence angle dependence of vertically polarized (V-pol) cross sections in good agreement with the composite surface model, but significant disagreement for horizontal polarization (H-pol) at  $X$  band. Comparisons of theoretical and measured Doppler spectra have been carried out by a number of authors [*Wright and Keller*, 1971; *Plant and Wright*, 1980; *Plant and Keller*, 1990; *Thompson et al.*, 1991]. *Plant and Keller* [1990] presented evidence for the dominance of Bragg scatter at mid-incidence by examining Doppler spectra. Similarly, *Thompson et al.* [1991] obtained good agreement between measured and modeled Doppler spectra of both V- and H-pol  $K_u$  band data at  $20^\circ$  incidence.

Perhaps the most difficult means of comparing theory and experiment is based on absolute measurements of the microwave backscatter, which are used to calibrate a model based on some assumed form or crude estimate of the water wave spectrum. Most papers in this category simply assert, or theoretically develop, some expression for the short wave elevation spectrum, merge it with measured values for the long wave spectrum, as did *Donelan and Pierson* [1987], and forge ahead. However, since some of the parameters used in the model functions are usually fits to microwave data, the models remain dependent on the very instruments whose accuracy they seek to verify. This choice of approach has been due mostly to the difficulty in measuring short wave spectral density, especially in two dimensions [*Apel*, 1994; *Banner et al.*, 1989; *Ebuchi et al.*, 1987; *Jähne*, 1989; *Jähne and Schultz*, 1992; *Klinke and Jähne*, 1992; *Waas and Jähne*, 1992]. *Jähne et al.* [1992] examine different systems that aim to solve this problem and discuss the strengths and weaknesses of each.

Historically, optical methods have been hampered by limitations in technology. *Cox* [1958] developed the first optical technique for measuring short wave slope spectra in a wave tank, using telescopes and photocells. *Wright and Keller* [1971] expanded from one-dimensional to two-dimensional wavenumber slope spectra in a wind-wave tank, which were measured and processed photographically. Microwave cross sections at 9.4 GHz and 24 GHz were input into the simple Bragg model to derive water wave spectra at a number of wavenumbers in the vicinity of the gravity-capillary transition region. Theory and experiment agreed to within a few dB, but the experimental conditions were severely limited by many factors such as the extremely short fetch (3.7 m), the limitation to one polarization (vertical), and the paucity of calibrated optical wavenumber spectra obtained with extreme difficulty in the days before easy access to computers. *Keller and Gotwols* [1983] substantially improved the optical system by incorporating digital data

acquisition and signal processing, as well as expanding the calibration technique. *Jähne and Riemer* [1990] used a system similar to that of *Keller and Gotwols* [1983], but added a second light source at  $90^\circ$  to the setup to simultaneously measure the cross-wind spectrum. *Van Halsema et al.* [1992] compared calibrated spectral densities from *Jähne's* system with  $X$  band  $\sigma_0$  from the same wind-wave flume using two-scale theory and obtained good agreement.

In this paper we continue the work started by *Wright and Keller* [1971] by accurately measuring two-dimensional slope spectra of centimeter and millimeter waves, and using these spectra in the simple Bragg scattering model and the composite surface model to predict the backscattered cross section. These predicted cross-sections from the optical data are then compared with values measured by  $X$  band and  $K_a$  band scatterometers under identical conditions. We do not attempt a comparison with the integral scattering models of *Holiday* [1987] and *Thompson* [1989], since they assumed infinite conductivity, which causes significant errors in the absolutely calibrated cross section.

## Experimental Configuration

### Wave Tank and Environmental Sensors

The wave tank used to obtain the measurements reported in this paper was recently described by *Keller et al.* [1992]; hence, we will give only an abbreviated description here. The tank was 30.5 m long, 2.4 m wide, and 90 cm deep. Figure 1 shows the measurement section of the wind-wave tank. From left to right are the microwave anechoic chamber, the mount for the environmental sensors and the CCD camera for the optical system, and the fixed-range, variable incidence angle arch with the  $X$  band and  $K_a$  band microwave systems. The microwave anechoic chamber was a unistrut framework holding styrofoam panels to which pyramidal microwave absorber was attached. The absorbing panels were suspended from the roof, the back, and the sides of the chamber. The chamber served to absorb any forward scatter from the microwave systems before the radiation could be reflected off other structures in the building back into the tank, then rereflected off the water into the antennas and contaminate the backscattered signal. This is the setup used for all the  $K_a$  band measurements, and for any  $X$  band data collected to check previous results. The sloped panels of microwave absorber under the optical/environmental mount were used during all the microwave measurements. The panels were removed when the optical system was in operation, since they blocked the camera's view of the water. Microwave measurements were not made at the same time as optical measurements. Throughout the measurements the water depth was maintained at approximately 44 cm, the height of the air tunnel at 46 cm, and the fetch at 16.3 m. While acquiring the optical data, 10-cm-thick

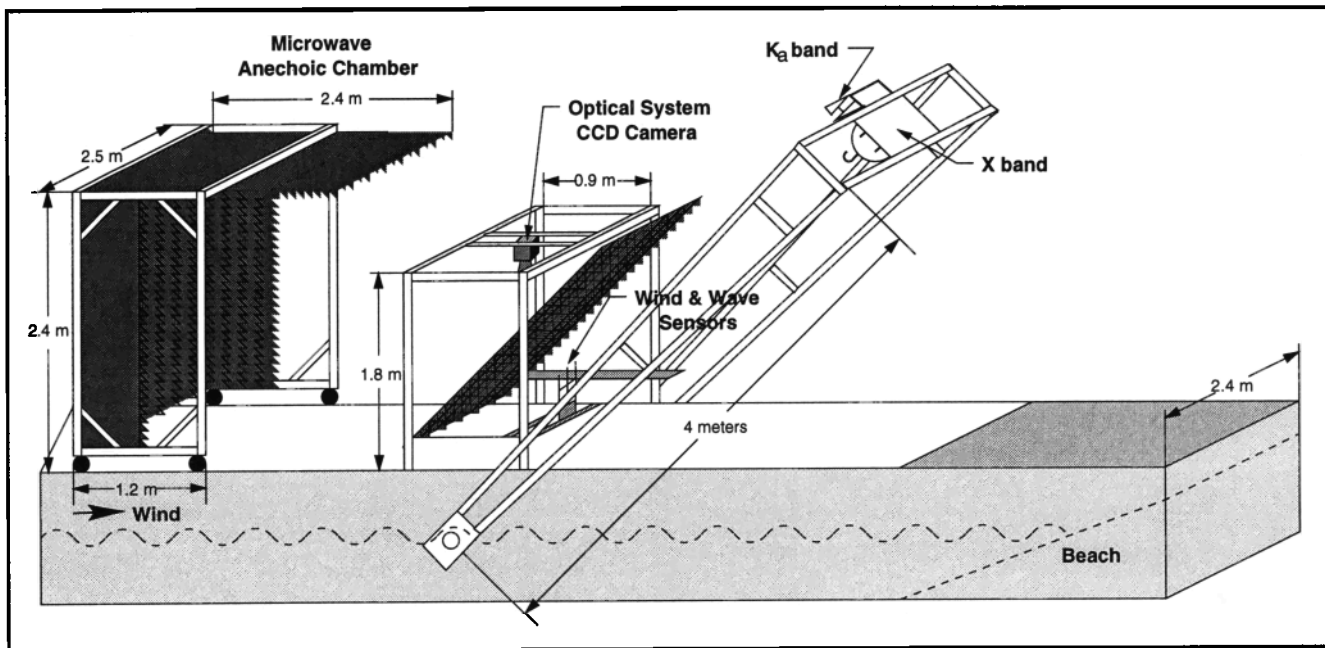


**Figure 1.** Representative drawing of 10 m of the wind-wave tank showing the measurement section as outfitted for  $K_a$  band microwave measurements. Not shown are 2.24 m by 2.24 m of microwave absorbing material placed on the air channel roof directly below the microwave systems to block any side-lobe scattering from waves in the tank.

styrofoam panels served as a roof for the air channel, and a clear plexiglass window (61 cm by 61 cm) was inserted in the roof directly below the camera to permit observation of the water, and to prevent disruption of the airflow. One section of the styrofoam tank roof, 4.5 m in length, was replaced during microwave measurements by thin clear plastic panels, which were found to be transparent to both  $X$  and  $K_a$  band radiation.

The environmental sensors are located in the same up/down tank position as the center of the optical/microwave measurement site, but offset 70 cm from the center of the tank, so as to be outside the scatterometer beam, as indicated in Figure 1. Mid wind tunnel wind speed is measured with a Pitot tube. Wind

stresses were measured 12 cm above the mean water level with crossed hot film anemometers, and calibrated against a Pitot tube located at the same height. Wave height was measured with a capacitance wave probe. Wind friction velocity,  $u_*$ , was varied over the range 10 – 120  $\text{cm s}^{-1}$ . This corresponds to 19.5 m neutral stability wind speeds of 2 – 25  $\text{m s}^{-1}$ . Details of the calibration of the crossed hot film anemometers, and conversion from  $u_*$  to  $U_{19.5}$  for this tank are given by Keller *et al.* [1992]. Typically, the wavelength of the dominant wind wave exceeded the baseline of our optical system, so we estimated it by measuring frequency spectra and converting the frequency of the spectral peak to wavenumber using the shallow water gravity wave dispersion relation, ignoring the wind-drift current. The results are shown in Figure 2, where peak wavelength is plotted against friction velocity,  $u_*$ .

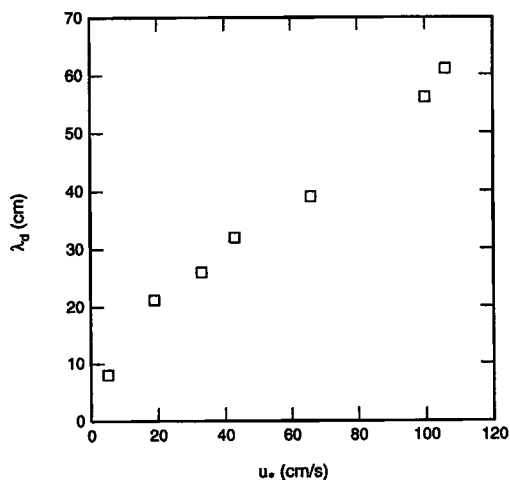


**Figure 2.** Wavelength of the dominant wind-wave,  $\lambda_d$ , versus wind friction velocity,  $u_*$ , in the wave tank. The fetch was 16.3 m.

### Optical Setup and Calibration

One component of vector wave slope is measured using the optical system illustrated in Figure 3a. The design has gradually evolved from the measurement of slope at a point by Cox [1958], to the slope measurements over an area by Wright and Keller [1971] and Keller and Gotwols [1983]. A similar arrangement using a different light source has been described by Jähne and Riemer [1990]. The scheme operates on the principle whereby light from a light source with a known spatial gradient under the water is refracted at the water surface and collected by a sensor located above the water. The light source consists of a xenon flash tube 50 cm in effective length. The full width at half maximum of the flash pulse was measured to be approximately 400  $\mu\text{s}$ .

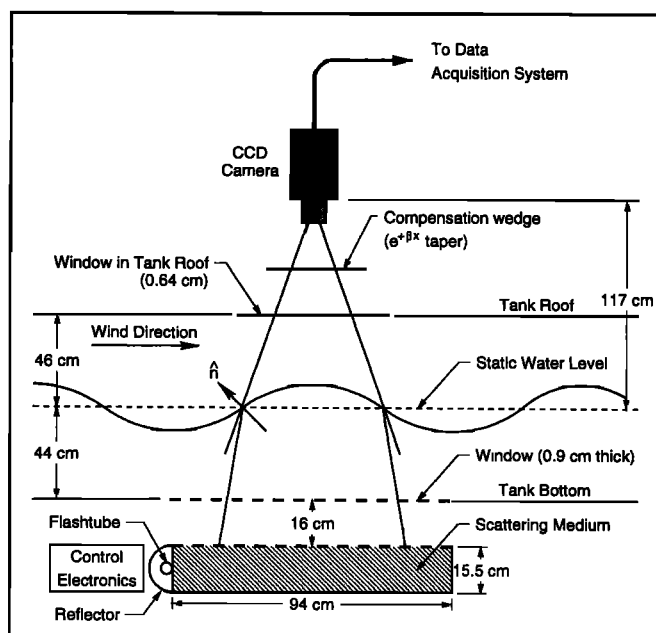


Figure 3a. Optical system used in the wave tank at a fetch of 16.3 m.

This is short enough to resolve the shortest wavelength (1-2 mm) waves imaged by this system without significant smearing. Light from the flash lamp is multiply scattered in a container of colloidal silica hydrosol. The radiance scattered vertically toward the water surface is exponentially attenuated with path length through the scattering medium. Tracing a typical ray upward through the air-water interface, we see a bending away from the local normal, passage through the compensation wedge, collection by the camera optics, and focus on a charge coupled device (CCD). For a given point in the image the ray path in air is fixed in space, but the ray underwater moves back and forth across the exponential gradient of the light source. It is this movement of the ray vector across the light source that causes the intensity of the recorded image to be an exponentially encoded version of the up/downwind component of waveslope.

Evidence for the accurate exponential nature of the scattering is shown in Figure 3b, where an up-tank/down-tank cut through the CCD image is compared with an exponential function with an  $e$ -folding scattering length of 20.3 cm. The minor fluctuations in the data are due to specks of dirt on both the light source and the window in the roof of the tank. In order to obtain the data in Figure 3b it was necessary to remove the compensation wedge from the optical train. In the presence of the compensation wedge the plot would be approximately a flat line. The purpose of the compensation wedge is to cancel the exponential gradient orthogonal to the light source in the absence of waves. This cancellation does not prevent the exponential encoding of slope when wind waves are present, but it does reduce the dynamic range needed to record the images. This is a highly desirable feature, since for some studies (not

the present one) the images are recorded on video tape with limited dynamic range of the order of 100:1.

The signal from the CCD camera (Fairchild model CCD 5000) is digitized in an 8 bit video frame grabber board (Matrox model PIP-1024A) located in an IBM PC/AT computer. The computer controls both the flashtube firing and the frame grabber; hence, it is possible to freeze the image corresponding to the flash pulse. The digitized signal is passed through a logarithmic lookup table built into the frame grabber. In order to linearize the radiance to slope transfer function it is necessary to know the dark level. This is measured at least once a day and appropriate changes are entered in the log lookup table. In practice, we have found that after a brief warmup period the dark level remains constant throughout a full day, with only very small changes from one day to the next. The accurate exponential nature of the light source, and the good stability of the entire system, make it possible to accurately linearize the measurements over the entire dynamic range of the instrument.

The linearized data are recorded in two ways. The two-dimensional images are converted back to analog form and recorded on U-Matic format video tape. In addition, each row of digital data in the crosswind direction is summed and the sum recorded on the computer's disk. This summation will be described in a later section; its purpose is to allow more accurate processing of the data than is possible when using video tape. It

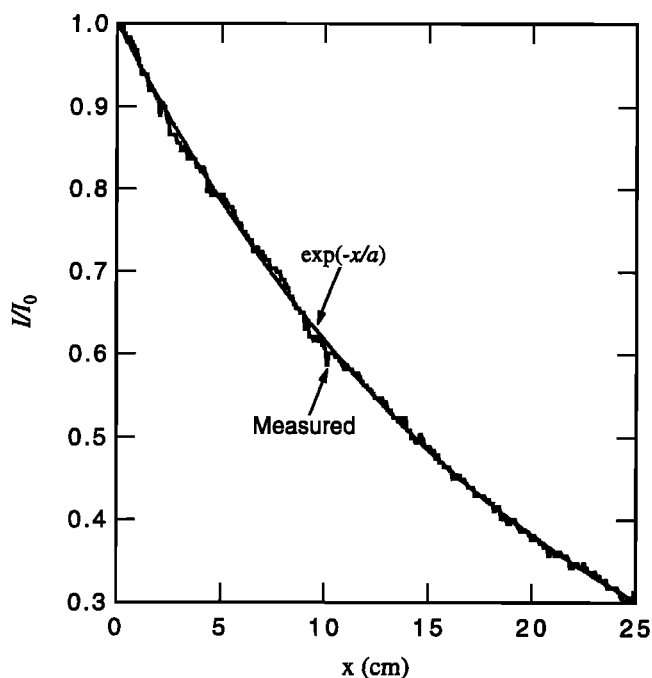


Figure 3b. Comparison of measured and fitted normalized intensity in the up-tank/down-tank direction from a CCD image of still water. The compensation wedge was removed from the optical train. The plot has been corrected for dark current. The scattering length,  $a$ , is 20.3 cm.

has the additional benefit that the data need not be converted back into an analog signal for storage on video tape. Thus it is the more accurate method for data storage, and wherever possible, we prefer these cross-tank summed data over the data stored on video tape.

Photometric calibrations are carried out by floating on the water an artificial wave made of clear plastic. The artificial wave consists of a triangle wave with  $\pm 15^\circ$  slope, resulting in an apparent square wave in the recorded data. Geometric calibrations are performed by floating a transparency on the water which has a pattern of known size printed on it. The image is 25 cm up/downwind by 34 cm crosswind. In order to reduce the effect of the finite length of the light source (50 cm) the analysis is constrained to cover the central 15.8 cm of the image in the crosswind direction. The corresponding number of picture elements analyzed is 240 up/downwind by 331 crosswind.

In order to measure the crosswind component of wave slope it is only necessary to rotate the light source by  $90^\circ$  and rerun the measurements. To date, we have not done this, preferring to concentrate on the more important up/downwind component to which the microwaves respond.

The largest upwind/downwind slope which can be imaged without the ray vector going off the light source is approximately  $81^\circ$  in the center of the imaged area, and  $68^\circ$  on the outer edges. Such large slopes are observed only occasionally in very small regions associated with microscale wave breaking, and they have not contributed significantly to the results presented in this paper.

The smallest slopes that can be imaged are determined by system noise. As will be discussed in the next section, we digitally sum the pixels in the cross-tank direction. This results in a significant improvement in the minimum detectable slope. For instance, at the lowest friction velocity reported in this paper,  $15 \text{ cm s}^{-1}$ , we find the signal to noise ratio, defined as the ratio of the variance of the slope signal to the variance of the system noise, to be a comfortable value of 193, or about 23 dB. With increasing wind, the signal to noise ratio improves further to about 30 dB.

### Optical Data Processing

Let  $\Psi(\vec{k})$  be the two-dimensional wavenumber spectral density of wave elevation  $\zeta$ :

$$\Psi(\vec{k}) = \frac{1}{(2\pi)^2} \int_{-\infty}^{+\infty} \int_{-\infty}^{+\infty} e^{i(\vec{k} \cdot \vec{x})} \langle \zeta(\xi, \eta, t) \zeta(\xi + x, \eta + y, t) \rangle dx dy \quad (1)$$

where angular brackets represent an ensemble average. The mean square elevation can be obtained by integrating over all  $\vec{k}$ :

$$\langle \zeta^2 \rangle = \int_{-\infty}^{+\infty} \int_{-\infty}^{+\infty} \Psi(\vec{k}) dk_x dk_y. \quad (2)$$

The slope component spectrum for the uptank/down-tank slope component  $s_x$  is given by

$$\Phi_x(\vec{k}) = \frac{1}{(2\pi)^2} \int_{-\infty}^{+\infty} \int_{-\infty}^{+\infty} e^{i(\vec{k} \cdot \vec{x})} \langle s_x(\xi, \eta, t) s_x(\xi + x, \eta + y, t) \rangle dx dy \quad (3)$$

which is related to the elevation spectrum by

$$\Phi_x(\vec{k}) = k_x^2 \Psi(\vec{k}) \quad (4)$$

where  $\Phi_x(\vec{k})$  can be estimated by computing the finite Fourier transform of the two-dimensional slope component image,

$$S_x(\vec{k}) = \frac{1}{L_x L_y} \int_{-L_x/2}^{+L_x/2} \int_{-L_y/2}^{+L_y/2} e^{i(\vec{k} \cdot \vec{x})} s_x(x, y) dx dy \quad (5)$$

and taking an ensemble average of squared magnitudes of  $N$  such transforms:

$$\Phi_x(\vec{k}) \approx \frac{1}{N} \sum_{n=0}^{N-1} \frac{|S_x(\vec{k}; n)|^2}{\Delta k_x \Delta k_y} \quad (6)$$

where  $\Delta k_x = 2\pi/L_x$  and  $\Delta k_y = 2\pi/L_y$ .

Since the microwave systems respond to Bragg waves traveling toward and away from the antenna, we do not need to compute the full two-dimensional transform, but can be satisfied with  $S_x(k_x, 0)$ .  $S_x(k_x, 0)$  can be computed by integration in the  $y$  direction, followed by a one-dimensional transform. This approach drastically reduces the data rate, making it feasible to record digital data and avoid the inaccuracies inherent in video tape recording.

The slope component  $q(x)$  integrated in the  $y$  direction (in practice, this has been in the crosswind direction) is given by

$$q(x) = \frac{1}{L_y} \int_{-L_y/2}^{+L_y/2} S_x(x, y) dy \quad (7)$$

Then

$$S_x(k_x, 0) = \frac{1}{L_x} \int_{-L_x/2}^{+L_x/2} e^{i(\vec{k} \cdot \vec{x})} q(x) dx \quad (8)$$

is a one-dimensional Fourier transform of the cross-tank integrated data. The quantity  $q(x)$  is computed during the interval between flashes, and saved on the computer's disk.

Calibration of  $q(x)$  involves subtraction of the  $q(x)$  profile measured in the absence of wind, and multiplication by the slope calibration scale factor. The quantity  $q(x)$  is preconditioned by subtracting a linear trend and any residual mean value which may be present. Following application of a Hanning window, a one-dimensional spectrum is computed using the fast Fourier transform (FFT) algorithm. The output of the FFT is squared, and the spectral estimates corrected for the effect of the

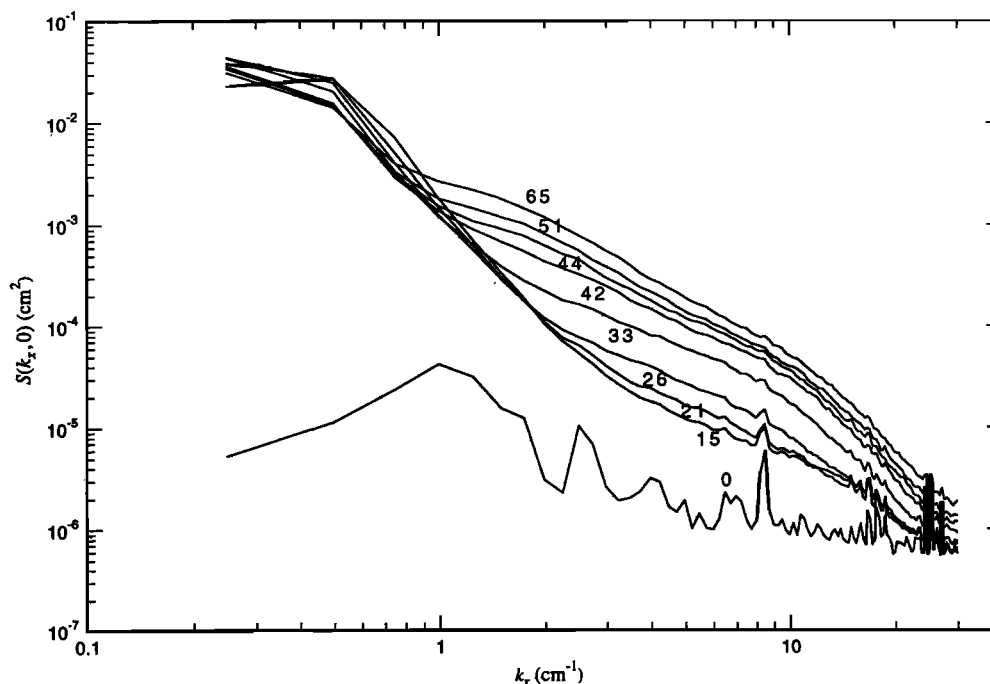


**Figure 4.** Uncorrected cross-tank integrated slope spectra versus wavenumber ( $k_x$ ) as a function of wind friction velocity. The zero level spectrum is shown at the bottom. The numbers are the corresponding friction velocity values in  $\text{cm s}^{-1}$ .

Hanning window by multiplying by the factor  $8/3$ . The two degree of freedom spectra are ensemble averaged, typically over 1800 members.

Figure 4 shows the uncorrected spectra derived from the crosstank integrated data used for the optical/microwave comparison. These data were collected during April 1988. The multitude of bumps are apparently caused by nonuniformity in the grid of picture elements of the CCD camera. At the lowest (nonzero)  $u_*$  the spectrum approaches a noise floor at the upper end of the wavenumber range. To correct for this noise floor, as well as the CCD artifacts, we subtract the still water spectrum from each of our spectral estimates. This correction is only important at wavelengths shorter than about 3 mm, and at wind friction velocity less than approximately  $20 \text{ cm s}^{-1}$ . The spectra for wavenumbers  $k > 16 \text{ cm s}^{-1}$  are too close to both the Nyquist frequency and the noise floor, and will therefore not be shown in subsequent figures.

### Microwave Systems Setup and Calibration

Coherent  $X$  and  $K_a$  band CW scatterometers illuminate areas that include the same area illuminated by the optical system. The  $X$  band system, which operates at 10.0 GHz (3.0 cm), is monostatic. The antenna is a single-polarization 61-cm parabolic dish mounted 2.9-m above the water surface, focused on the surface and operated, for this study, at incidence angles of  $28^\circ$ ,  $48^\circ$ , and  $68^\circ$ . Data were taken at VV (vertical transmit, vertical receive) and HH (horizontal transmit, horizontal receive) polarization by rotating the antenna. The 3-dB

level in the antenna pattern is roughly an ellipse at the mean water level. At  $45^\circ$  incidence angle, the dimensions are 26-cm upwind-downwind by 18-cm crosswind. This corresponds to a two-way half power beamwidth of  $2.7^\circ$ . The received signal is mixed down to an intermediate frequency of 400 Hz, and square law detected. The square law detected signal is low-pass filtered by a 24 dB/octave filter with a 1-Hz (3 dB) cutoff frequency. This signal, which is proportional to the backscattered cross section, is digitized with a 12 bit analog to digital converter, and stored on a Digital Equipment Corporation MINC-11CA computer. Absolute calibration of the scatterometer is carried out with a copper-coated sphere. Further details can be found in Keller *et al.* [1992].

The  $K_a$  band scatterometer operates at 35.0 GHz (8 mm), and is of a completely different design than the  $X$  band scatterometer. A schematic of the system is given in Figure 5. The IF cross-polarization signal was not used in this study. A pair of antennas, one for transmitting and one for receiving, are located side by side on a platform mounted above the  $X$  band dish. The scatterometers had been moved from the fixed height mount used by Keller *et al.* [1992] to a new fixed range ( $\sim 4 \text{ m}$ ), variable incidence angle arch in June 1990. This new experimental configuration is as shown in Figure 1. The transmitting antenna is a single polarization scalar horn, 7.5 cm in diameter; while the receiving antenna is a 15-cm dual-polarization scalar horn. For this study, only VV polarization was used, and the scatterometer was operated at incidence angles of  $36^\circ$  and  $59^\circ$ . The antennas' combined two-way beamwidth is  $4.0^\circ$ ,

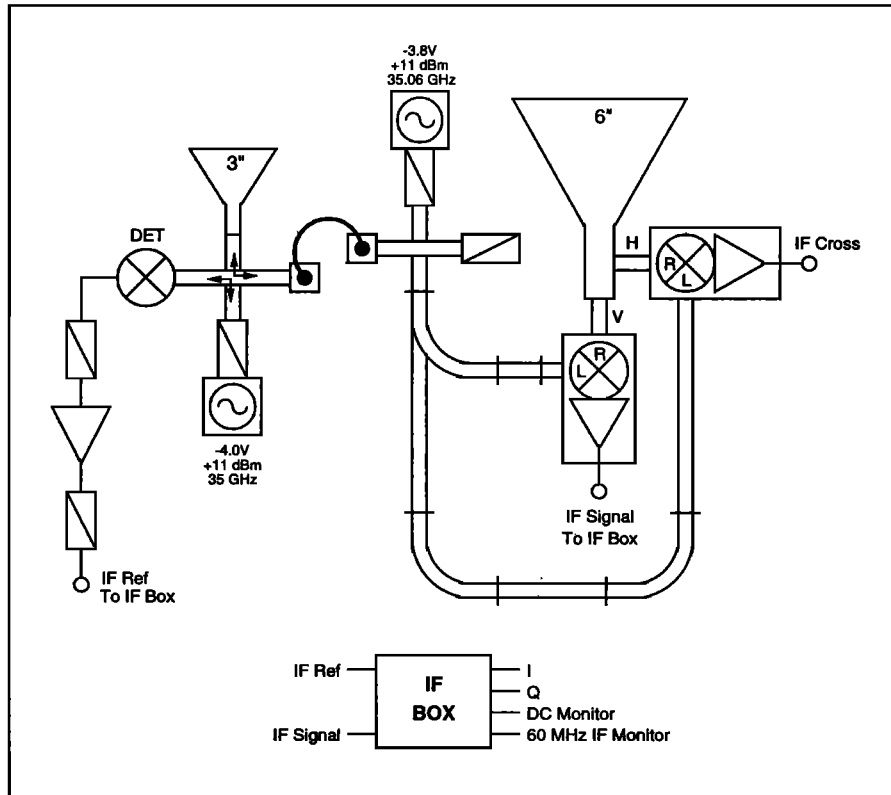


Figure 5. Block diagram of the 35 GHz scatterometer.

yielding, at the 3-dB level, an elliptical illuminated area at the mean water level at 36° incidence angle, of 33 cm up/downwind, by 25 cm crosswind. The receiver output consists of the received field beat down to an intermediate carrier frequency of 60 MHz, which is separated into in-phase and quadrature-phase (I and Q) signals in

the IF section. The I and Q signals are sampled at a 3 KHz rate, and are digitized to 12 bit precision on a PC/AT computer. The raw data are later transferred to another PC, where the backscattered cross-section, which is proportional to  $I^2 + Q^2$ , is computed.

The calibration procedure is as discussed by Keller *et al.* [1992], with the exception that changes to the mounting of the microwave systems meant that sliding ball calibrations became unwieldy to perform. Antenna pattern measurements were instead performed more frequently

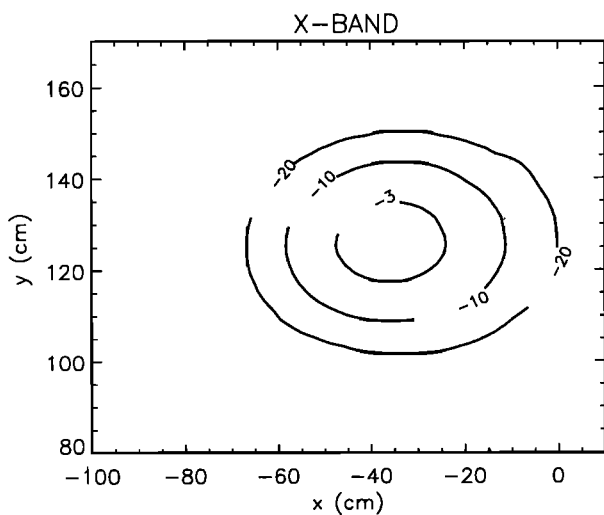


Figure 6a. Measured antenna pattern for the 10 GHz scatterometer at V-pol, 45° incidence, 3.89-m range. The  $x$  and  $y$  distances refer to a fixed point at the side of the tank. The  $x$  is positive in the upwind direction,  $y$  is positive in the crosstank direction. The numbers indicate the -3, -10, and -20 dB contours, where 0 dB is the peak power from the sphere.

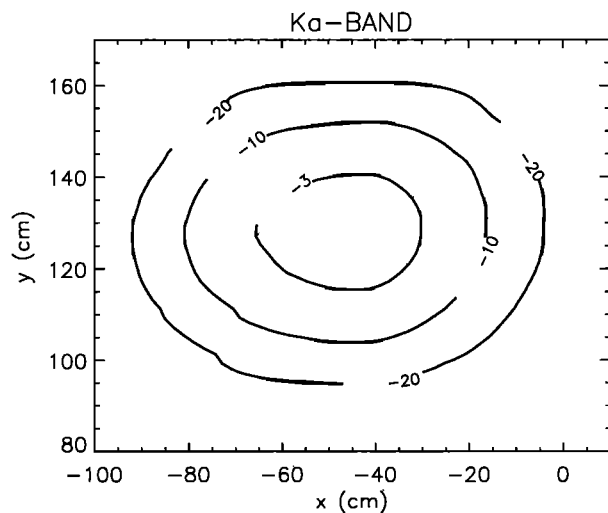


Figure 6b. Same as Figure 6a but for the 35 GHz scatterometer at V-pol, 36° incidence, 4-m range.

to track system drift, and also to estimate repeatability of our calibration technique. For both systems, the antenna patterns were measured with the moving, copper-coated ball mechanism, with results as shown in Figures 6a and 6b. As before, the carriage was moved from one side of the tank to the other, but in 4-cm steps at the extremes of the pattern, and in 2-cm steps in the center, where the pattern changes most rapidly. Further, we made repeated measurements at a given range and incidence angle, from which the calibrations were determined to be good to  $\pm 2$  dB at  $X$  band, and  $\pm 1.5$  dB at  $K_a$  band.

## Results

### Slope Component Images

Figure 7 presents a selection of slope component images at  $u_*$  of 15, 33, and 65  $\text{cm s}^{-1}$ . The images on

the left were chosen at random and should therefore be considered to be "typical." The images on the right were chosen to illustrate some particular features discussed below. At the lowest  $u_*$  (Figures 7a and 7b) the most prominent feature is the presence of steep capillary waves with wavelengths of the order of 1 cm. These capillaries are typically parasitic to a longer gravity wave which is sometimes hard to detect in the images, since its wavelength is of the order of or longer than the baseline imaged. Perhaps the most important observation that can be made is that the capillary waves are quite steep where they exist, but, as Figure 7b shows, there are large regions that appear to be completely devoid of waves of this scale. Furthermore when it is recognized that the microwave systems respond mainly to only those components of the capillary waves which are aligned parallel to the  $x$  axis (vertical in the figure), it is evident that the  $K_a$  band microwave signal will be quite sporadic in

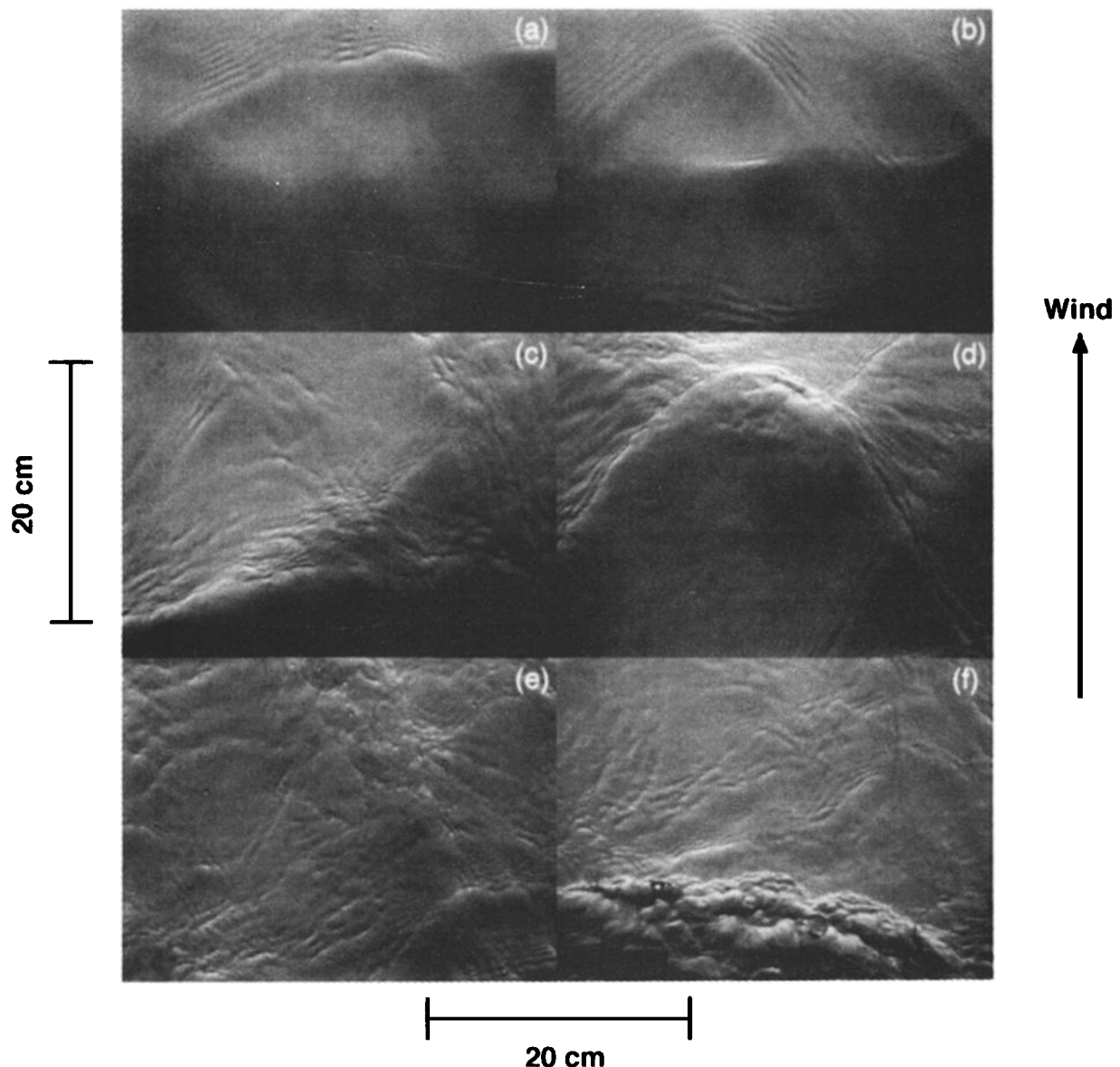


**Figure 7.** Slope component images at various  $u_*$ : (a and b)  $15.5 \text{ cm s}^{-1}$ , (c and d)  $33.1 \text{ cm s}^{-1}$ , and (e and f)  $64.7 \text{ cm s}^{-1}$ .

nature, appearing as a series of spikes rather than a continuous signal. A more detailed discussion of the statistics of the backscattered cross section measured in the same wave tank is given by *Gotwols and Keller* [1990].

At medium  $u_*$  (Figures 7c and 7d) the surface takes on a more disorganized appearance. The parasitic capillaries now seem to coexist with abundant short crested waves which cover a wider percentage of the area than at low  $u_*$ . Slopes can be quite high in isolated regions, as at the top center of Figure 7d, but there is no evidence of breaking.

At high  $u_*$  (Figures 7e and 7f) the well-organized parasitic capillaries have given way to completely disorganized waveforms which almost completely fill the space. Occasional breaking or near-breaking events such as shown in Figure 7f exhibit dramatic slope changes over a scale of less than 1 cm. Bubbles also become common. Individual bubbles are remarkably long lived in this freshwater tank, propagating a meter or more down wind before dissipating. There are only occasional regions of smooth water, and these usually follow behind a breaking wave.

**Optical spectra**

Cuts through the two-dimensional spectra in the upwind/downwind direction are shown in Figure 8. The spectra have been corrected for instrumental noise by subtracting the still water spectrum. Since the Hanning windowing procedure corrupts the spectrum at the wavelength corresponding to the baseline of the measurements, the lowest wavenumber plotted is the second

harmonic of the image baseline, and the highest wavenumber shown is well below the Nyquist limit. Three regimes are apparent. At low wavenumber the spectra fall rapidly, approximately as  $k^{-4}$ . This steep slope, corresponding to  $k^{-6}$  in the wave height spectrum, is caused by the so-called peak enhancement effect common to all wave tanks, where the dominant wind wave is considerably steeper than found on the open ocean. As  $u_*$  increases, this region migrates to lower wavenumbers. Had our tank been longer, this range would have been off the left end of the graph at all  $u_*$ ; hence we will not discuss this regime further. In the middle of the wavenumber range, the equilibrium range [*Kitaigorodski*, 1993; *Phillips*, 1958, 1985], the rate of falloff decreases, lying within the range of approximately  $k^{-1.5}$  to  $k^{-2}$ . At large wavenumber the slope steepens again, declining as steeply as  $k^{-5}$ , but appearing to curve over to an even steeper falloff at wavenumbers higher than shown.

We have computed a least squares linear fit of the log of the upwind/downwind slope spectral density in a  $\pm 12.5\%$  bandwidth centered on wavenumbers corresponding to the  $X$  and  $K_a$  band Bragg resonance conditions at  $48^\circ$  and  $59^\circ$ , respectively. The resulting spectral indices,  $n$  (corresponding to  $k^{-n}$ ), are shown in Figure 9. At  $X$  band two points at the lowest  $u_*$  are contaminated by the peak enhancement effect and therefore should be ignored. The remainder of the points indicate that the spectrum gradually steepens with increasing  $u_*$ . At  $K_a$  band the spectra rapidly steepen with  $u_*$ , reaching a peak of about -3.3, then begin a slow recovery to about -2.9 at the highest friction velocity.

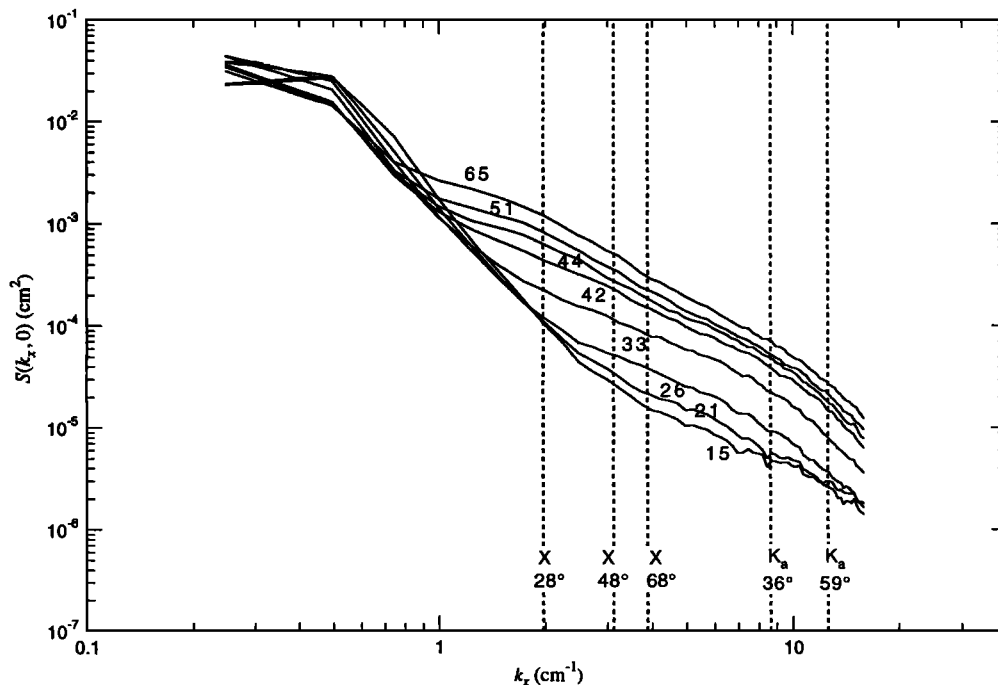


**Figure 8.** Corrected crosstank integrated slope spectra versus wavenumber ( $k_x$ ) as a function of wind friction velocity. The numbers are the corresponding friction velocity values in  $\text{cm s}^{-1}$ . The dotted vertical lines indicate the Bragg wavenumber for the given frequency and incidence angle.

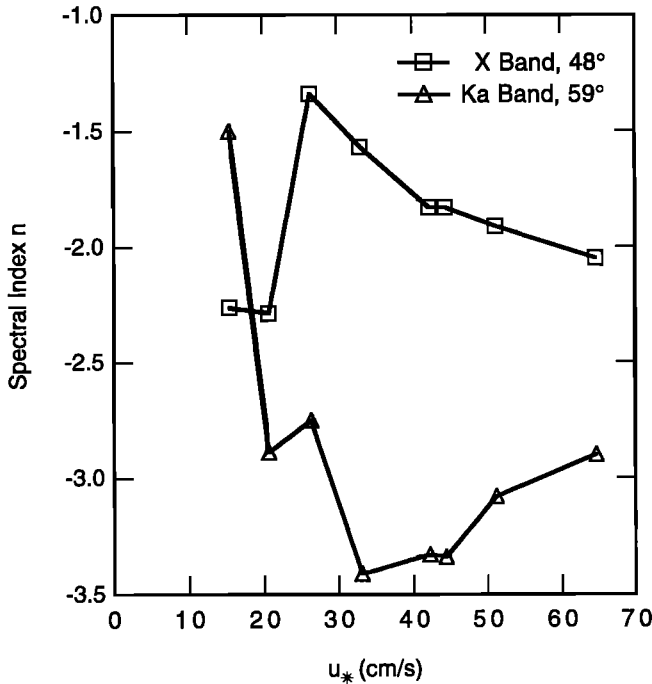


**Figure 9.** Spectral index at the microwave  $X$  and  $K_a$  band Bragg resonance wavenumbers of  $3.1$  and  $12.6 \text{ cm}^{-1}$ , which are the Bragg resonant wavenumbers for  $48^\circ$  and  $59^\circ$ , respectively.

### Microwave System Results

Because of microwave reflections from the edges of the window in the air channel roof through which the CCD in the optical system viewed the water, we were not able to make microwave and optical measurements simultaneously. Many researchers have reported  $\sigma_0$  at  $X$  band, and since the  $X$  band tank scatterometer had yielded substantial, repeatable data (within 3 dB) for a broad range of incidence angles, we chose, rather than to repeat all the  $X$  band measurements for this paper, simply to use the data, collected without plastic partially blocking the airflow, from Keller *et al.* [1992] for the  $X$  band comparison. However, we did repeat some measurements at  $48^\circ$ , V-pol, and  $68^\circ$ , V- and H-pols, to verify or supplement previous results.

Since we wanted to compare the optical spectra to backscatter values higher in the optical system's wave-number range, 35 GHz, in the same clear atmospheric window, but above the liquid water line at 22 GHz, was chosen for companion operation. According to Bragg theory, the  $K_a$  band scatterometer would be in resonance with capillary waves in the 5-mm to 1-cm wavelength range, where very little is understood, or even, where there were few previous measurements against which to compare [Grant and Yaplee, 1957, Masuko *et al.*, 1986, and Witting and Wright, 1975]. The V-pol  $K_a$  band data were acquired at  $36^\circ$  and  $59^\circ$ , in July and August of 1991, and May and December of 1992, respectively, and are presented here for the first time.

### Microwave/Optical Comparison

In order to compare the optical and microwave measurements, data from the microwave and optical systems must be converted to a common variable through some model which relates the respective measurements. We have used both Bragg scattering and composite surface theory to make this conversion. The Bragg relationship is given by

$$\sigma_0 = 16\pi k_0^4 |g(\theta)|^2 \Psi(2k_0 \sin \theta, 0) \quad (9)$$

where  $k_0$  is the microwave number,  $\theta$  is the incidence angle, and  $g(\theta)$  for both polarizations is given by Plant [1990].

Using this expression along with the optical measurements of  $\Phi_x(k_x, 0)$  evaluated at  $k_x = 2k_0 \sin \theta$ , we then computed  $\sigma_0$  for comparison with the microwave measurements. Van Halsema *et al.* [1992] performed a similar analysis with data from a 100-m wind-wave flume, but used only an  $X$  band system. They found good agreement at V-pol across a wide range of incidence angles and friction velocities, but that at H-pol, the measured cross-sections were higher than the calculated values by about 5 dB at  $60^\circ$  incidence.

In developing the composite surface model to use with the optical data, we followed the theory and equations of Wright [1968], as amplified by Plant [1990]. The full composite scattering calculation was written as follows [cf. Wright, 1968, equations 10-17]:

$$\sigma_0 \cong 16\pi k_0^4 \int_{-\infty}^{+\infty} \int_{-\infty}^{+\infty} |G(\theta, \alpha, \phi)|^2 \Psi(2k_0 \sin \theta', 0) P(\alpha, \phi) d\alpha d\phi \quad (10)$$

where

$$G_{VV} \cong g_{vv}(\theta')$$

$$G_{HH} \cong g_{hh}(\theta') + (\tan^2 \phi \csc^2 \theta') g_{vv}(\theta')$$

$$g_{vv} = \frac{(\epsilon - 1) [\epsilon(1 + \sin^2 \theta') - \sin^2 \theta'] \cos^2 \theta'}{[\epsilon \cos \theta' + \sqrt{\epsilon - \sin^2 \theta'}]^2}$$

$$g_{hh} = \frac{(\epsilon - 1) \cos^2 \theta'}{[\cos \theta' + \sqrt{\epsilon - \sin^2 \theta'}]^2}$$

$$\epsilon = \frac{\epsilon_w}{\epsilon_0}$$

$\theta' \cong \theta + \alpha$ , is the local incidence angle,  $\alpha$  is the up-wind/downwind slope perturbation angle,  $\phi$  is the cross-wind slope perturbation angle,  $\epsilon_w$  is the permittivity of water, and  $\epsilon_0$  is the permittivity of free space.

In the slope probability distribution function,  $P$ , Wright approximated the tangents of the perturbing angles by the angles themselves, and assumed the up-

wind/downwind and crosswind components had equal weight, and that the distribution was Gaussian. Thus,

$$P(\phi, \alpha) = \frac{1}{2\pi S^2} e^{-(\phi^2 + \alpha^2)/2S^2} \quad (11)$$

where  $S^2$  is the mean-squared slope of the long waves. The expressions Wright used for  $g_{vv}$  and  $g_{hh}$  are given by Plant [1990] in equations 4.46 and 4.47.

Valenzuela [1978] derived his own forms for the composite surface model that differ slightly from the Wright expressions (cf. equations 4.5, 4.6, 4.7, 5.1, 5.2, 5.3):

$$\begin{aligned} \sigma_0 &\cong 16\pi k_0^4 \int_{-\infty}^{+\infty} \int_{-\infty}^{+\infty} \cos^4 \theta' |G(\theta, \alpha, \phi)|^2 \\ &W(k_0, \theta, \alpha, \phi) \\ &P(\tan \alpha, \tan \phi) d \tan \alpha d \tan \phi \end{aligned} \quad (12)$$

where

$$\begin{aligned} W &\cong \Psi(2k_0 \sin \theta', 2k_0 \cos(\theta + \alpha) \sin \phi) \\ G_{VV} &\cong (\sin(\theta + \alpha) \cos \phi \csc \theta')^2 g'_{vv}(\theta') \\ &+ (\sin \phi \csc \theta')^2 g'_{hh}(\theta') \\ G_{HH} &\cong (\sin(\theta + \alpha) \cos \phi \csc \theta')^2 g'_{hh}(\theta') \\ &+ (\sin \phi \csc \theta')^2 g'_{vv}(\theta') \\ g'_{vv} &= \frac{(\epsilon - 1) [\epsilon(1 + \sin^2 \theta') - \sin^2 \theta']}{[\epsilon \cos \theta' + \sqrt{\epsilon - \sin^2 \theta'}]^2} \\ g'_{hh} &= \frac{(\epsilon - 1)}{[\cos \theta' + \sqrt{\epsilon - \sin^2 \theta'}]^2} \end{aligned}$$

and  $\theta' \cong \arccos(\cos(\theta + \alpha) \cos \phi)$ .

Note that the  $\cos^4 \theta'$  has been moved out of the  $G$  function expression. The Wright expressions for  $g'_{vv}$  and  $g'_{hh}$  and Valenzuela expressions for  $g_{vv}$  and  $g_{hh}$  differ only by a  $\cos^2 \theta'$  factor. Valenzuela left the upwind/downwind and crosswind components separate in the slope probability expression:

$$P(\tan \phi, \tan \alpha) = \frac{1}{2\pi S_u S_c} e^{-[\tan^2 \phi / 2S_c^2 + \tan^2 \alpha / 2S_u^2]} \quad (13)$$

where  $S_u$  and  $S_c$  are the upwind/downwind and crosswind components of the slope variance, evaluated at the instantaneous incidence angle,  $\theta'$ . The Valenzuela expressions have been used by various authors in the past [Durdan and Vesecky, 1985; Donelan and Pierson, 1987] to develop  $\sigma_0$  model functions. In the interest of completeness, the differences between the two composite surface models were compared, as will be discussed later in this section.

One problem in using a composite surface model is the determination of the mean squared slope variance, both upwind/downwind and crosswind, as a function of the Bragg cutoff wavelength, which is usually some multiple of the Bragg wavelength itself. Wright [1968] used the mean squared upwind/downwind slope measurements of Cox and Munk [1954] to make his original calculations. Donelan and Pierson [1987] calculated the required terms from their merged expression for the full spectrum. In this study, we have data which allow us to determine the relevant upwind/downwind mean-squared slope as a function of the cutoff wavelength and the friction velocity. We chose to take three times the Bragg wavelength,  $\lambda_B$ , to be the cutoff wavelength where:

$$\lambda_B = \frac{\pi}{k_0 \sin \theta}$$

The optical system yields an upwind/downwind slope spectrum every 5 s. The longest wavelength the optical system can resolve is one half of the patch on the water, or about 12 cm. However, each element of the CCD camera responds to slope changes from all wavelength of waves in the tank. A single point system, as each CCD element is, cannot be resolved in wavenumber, but can be used to generate a total slope variance (Note that although we require the mean squared slope component,  $S_u^2$ , due to difficulties in calibration we can only measure the slope component variance. Since the mean slope is small in the tank, we can use the two interchangeably.) To obtain the relevant upwind/downwind slope variance is simply a matter of integrating the variance at any crosstank integrated point, and subtracting the integral of the spectrum obtained from the total system below  $3\lambda_B$ . We used this procedure to get one realization of  $S_u^2$  for various values of  $\theta$  and  $u_*$ . Thus we avoid problems at long wavenumber due to detrending the data by computing the total variance of the up-

Table 1. Slope Variance ( $\times 10^{-3}$ )

$u_*$ , cm s <sup>-1</sup>	$3\lambda_B$ , cm				
	9.61	6.02	4.86	2.22	1.48
15.5	6.5	7.5	7.8	8.0	8.0
20.7	10.0	10.7	11.0	11.1	11.1
26.4	13.0	13.6	13.8	13.9	14.0
33.1	17.9	18.3	18.5	18.8	18.8
42.2	22.7	23.1	23.3	23.8	24.0
44.4	26.7	27.1	27.3	28.0	28.2
51.2	29.2	29.6	29.9	30.8	31.0
64.7	33.3	33.9	34.3	35.5	35.8

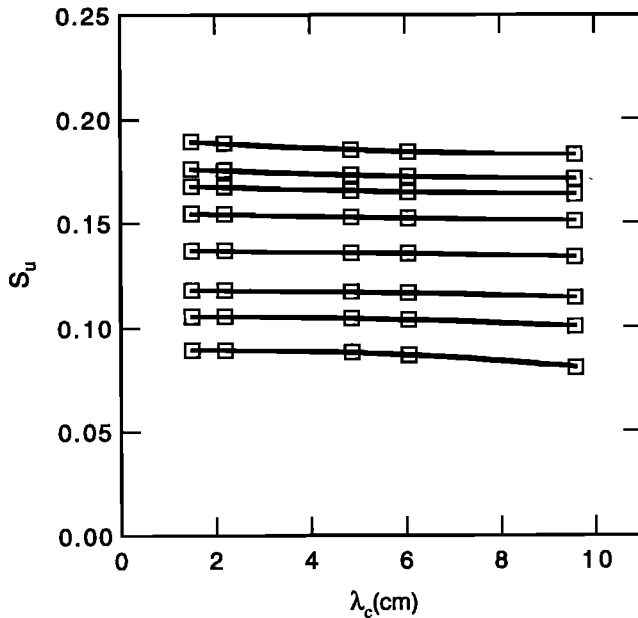


**Figure 10.** Root mean squared upwind/downwind longwave slope as a function of cutoff wavelength  $\lambda_c (= 3\lambda_B)$  and  $u_*$ , where the friction velocity values are 15, 21, 26, 33, 42, 43, 51, and 65  $\text{cm s}^{-1}$ , from bottom to top.

wind/downwind slope (after crosstank integration) and subtracting the integral of the spectral density below  $3\lambda_B$ . Over a 3-hour period, we were able to average over 1800 such values to obtain a very stable determination of  $S_u^2$  for use in the composite surface theory. The results for eight different  $u_*$  values and all five of our different Bragg wavenumbers are given in Table 1. From these 40 values, best fit polynomials were derived so the mean squared slopes would not have to be recalculated for every  $\theta_i$  used in the double integration. Figure 10 shows the root mean squared longwave slope as a function of  $3\lambda_B$  and  $u_*$ . The root mean squared slopes are higher than the values of Cox and Munk [1954], especially at low winds, but this may be due to greater inaccuracies in the sun glitter measurements at low winds than at high, and also due to the steeper slopes found in the tank than in the ocean. The root mean squared slope values agreed well with those calculated from the Donelan and Pierson model, which are based on both open ocean and lake conditions, and which the authors noted are a factor of 1.7 higher than the Cox and Munk values.

However, these values are only the upwind/downwind values. For the slope probability term, a crosswind component is required. From previous tank work, the upwind to crosswind variance ratio was estimated to be about 3:1, as was discussed by Keller *et al.* [1992], so for the slope probability, the optical model used is

$$P(\phi, \alpha) = \frac{\sqrt{3}}{2\pi S_u^2} e^{-[3 \tan^2 \phi / 2S_u^2 + \tan^2 \alpha / 2S_u^2]} \quad (14)$$

where, as before,  $S_u$  is evaluated at the instantaneous incidence angle. Finally, while the limits of integration are  $\pm\infty$  in theory, eventually, when the perturbation angles are large enough,  $P(\phi, \alpha)$  becomes too small for the integrand to contribute significantly to the final composite value. Thus, the integration limits were set to be those values of the perturbation angles at which  $P(\phi, \alpha)$  fell below 1% of the maximum value of  $P$  at  $P(0, 0)$ . A similar limit was used in the Donelan and Pierson model function (original FORTRAN program kindly provided by W. J. Pierson). Further, varying the upwind/crosswind ratio from 3:1, while affecting  $P$ , had little effect on the resulting  $\sigma_0$ . In fact, far larger changes in  $\sigma_0$  could be obtained by varying the integration limits.

As was indicated earlier, the Wright and Valenzuela models differ most in the expressions each uses for  $|G|^2$ . If the perturbation angles are set to zero, the expressions are identical; however, as the perturbation angles increase, as they do for a full composite surface model calculation, the two expressions diverge. The composite surface model was programmed using both the Wright and Valenzuela expressions. The Valenzuela expression actually programmed was slightly different from equation (12) in that the crosswind component of the spectrum was set to zero, since that was not measured by the optical system. Predictions of the Wright and Valenzuela expressions differed by less than 1 dB. This difference is incorporated into the uncertainties in the composite surface results shown below.

Figures 11 and 12 show the principal result of this investigation. There, measured  $X$  and  $K_a$  band  $\sigma_0$  are compared with those computed using the optically derived wave height variance spectra. The solid lines and squares in this figure show cross sections computed from pure Bragg theory given by (9), while the solid lines and triangles show the results of the composite surface calculations given by (10) and (14). Optically derived spectral densities have been extracted from the spectra in Figure 8 at the nominal  $X$  and  $K_a$  band Bragg wavelengths and averaged across a  $\pm 12.5\%$  wavenumber range while simultaneously correcting for the  $k^{-n}$  drop-off for the pure Bragg calculations. The error bars represent the variability in the calibrations:  $\pm 2$  dB for the  $X$  band,  $\pm 1.5$  dB for the  $K_a$  band,  $\pm 1.5$  dB for the simple Bragg calculations, and  $\pm 2.5$  dB for the composite surface calculations, with the additional uncertainties mentioned above. These are not the 95% confidence intervals in the data shown in Figures 6b-13b and 18 of Keller *et al.* [1992], but are the variations in the calibration coefficient used to convert returned power to  $\sigma_0$ . The variations in the calibration coefficient were found by repeating antenna patterns at the same incidence angle and range at different times during acquisition of  $\sigma_0$  values. Repeated calibrations of the optical system, using the  $\pm 15^\circ$  wedge, were similarly performed during acquisition of the optical spectra, and could be used to determine how the calibration coefficient for that

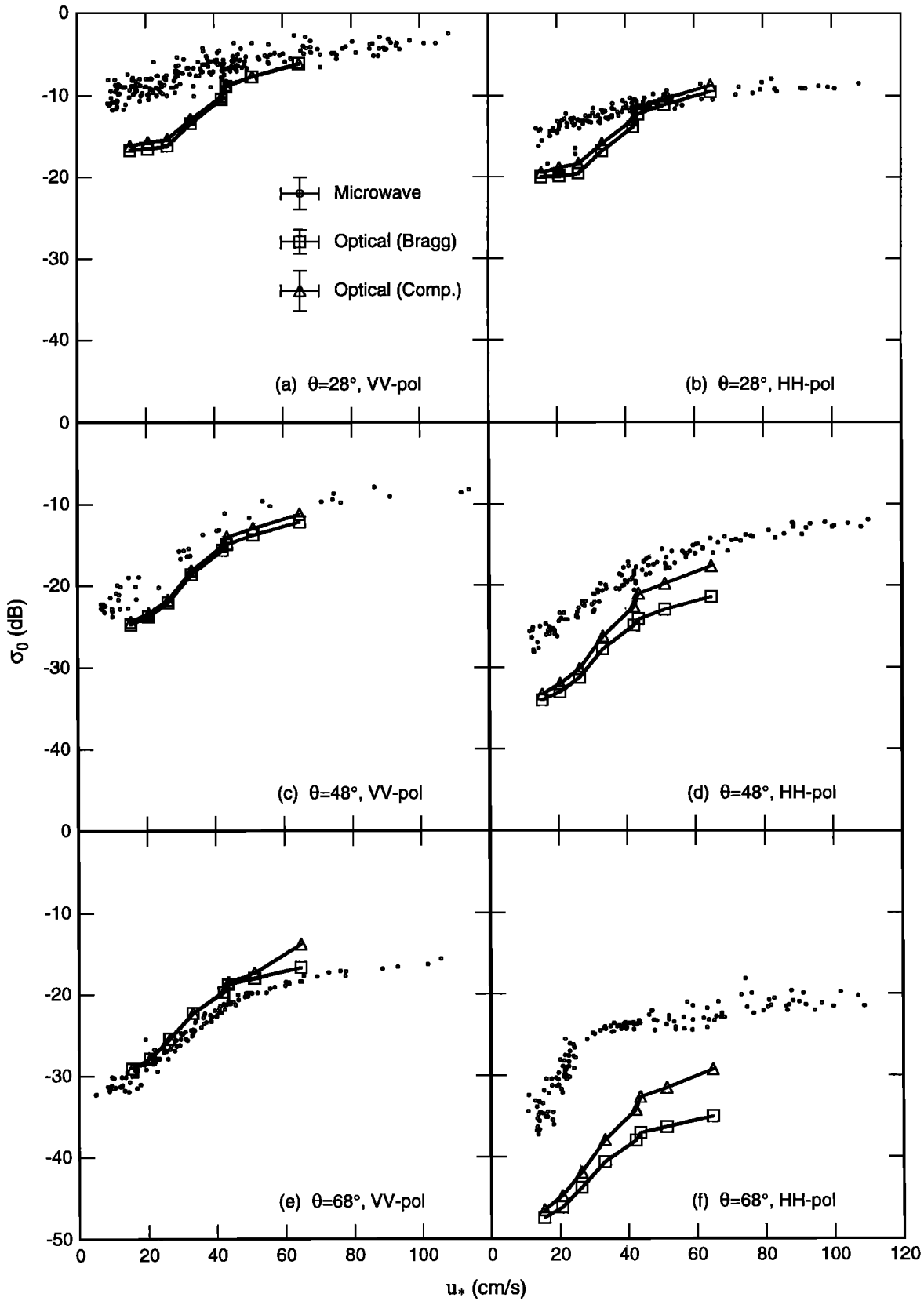


**Figure 11.** Microwave cross sections versus friction velocity for X band at the indicated incidence angles and polarizations. Open circles are measurements. Solid lines and squares are Bragg scattering predictions using optically-derived waveheight variance spectral densities. Solid lines and triangles are composite surface theory results using the same spectral densities. Representative error bars are shown in figure(a). Horizontal bars represent calibration variations in hot films. Vertical bars represent variations due to systems calibration and calculation approximations.

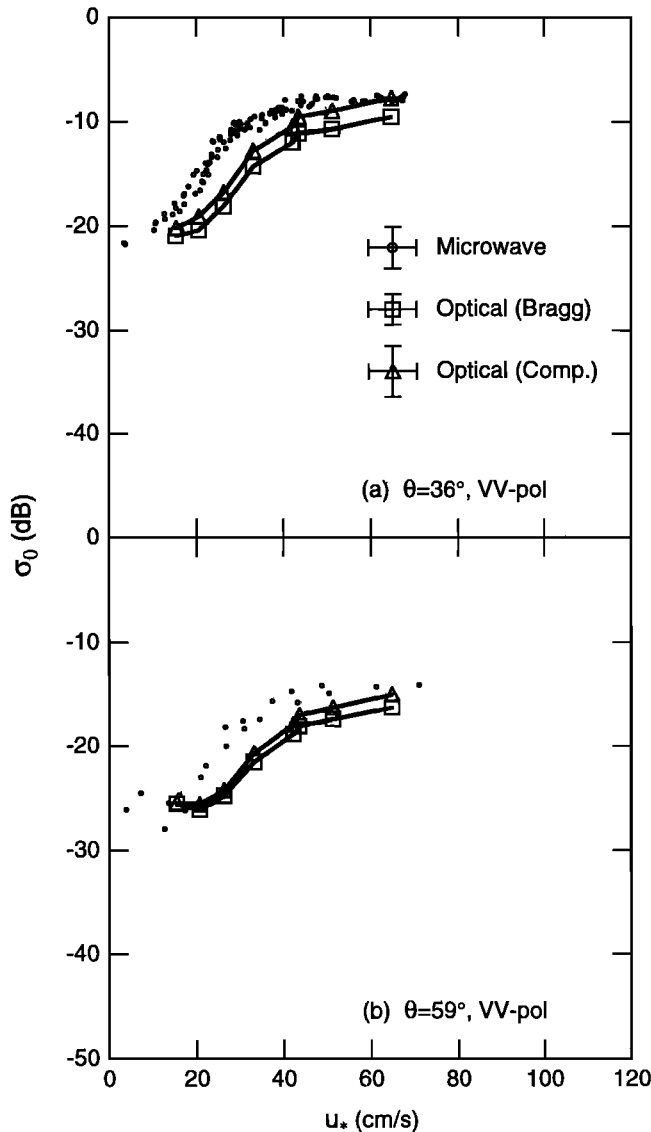


Figure 12. Same as Figure 11 but for  $K_a$  band V-pol at the indicated incidence angles.

system varied, as well. The error bars on the  $u_*$  are determined by taking the average Pitot tube variability measured by Keller *et al.* [1992] of  $\pm 0.6064 \text{ m s}^{-1}$  and calculating how the derived calibration coefficients would change. The average fluctuation in the hot film calibration yielded an overall variation of  $\pm 5.5 \text{ cm s}^{-1}$ .

The two figures show that composite surface theory generally fits the measured  $\sigma_0$  a bit better than pure Bragg scattering theory. In general, however, composite surface theory seems to predict cross sections which are somewhat smaller than those observed. The disagreement is frequently more for  $u_*$  between 20 and 40  $\text{cm s}^{-1}$  than for lower or higher values of friction velocity. Exceptions to this rule are X band  $\sigma_0$  for both polarizations at  $28^\circ$  and  $68^\circ$  incidence. At  $68^\circ$ , composite surface theory predicts slightly larger  $\sigma_0$  than are actually observed for V-pol, but much smaller ones than observed for H-pol. The reason for the overprediction at V-pol is not obvious at this time. At  $28^\circ$ , composite

surface theory agrees well with the microwave measurements above 40  $\text{cm s}^{-1}$  but not below it. In view of the rather good agreement observed at higher  $u_*$ , we do not believe that the discrepancies at  $28^\circ$  can be explained by calibration error in either the microwave or optical systems. It is possible that extraneous microwave scattering from the tank is responsible for the disagreement, although we attempted to take every precaution against this possibility. Figure 13a shows an X band Doppler spectrum obtained at  $28^\circ$  V-pol for a  $u_*$  of 15  $\text{cm s}^{-1}$ . The measured Bragg peak occurs at the equivalent of 8.76 Hz, while theory predicts a peak of 9.07 Hz, using the equations of Plant and Wright [1980]. This spectrum is a sample of a large set that was collected simultaneously with the  $28^\circ$  V-pol  $\sigma_0$  data using a real-time spectrum analyzer and analog plotter. The absence of any unidentifiable spectral peaks reinforces our conclusion that the microwave backscatter should be due mostly to composite surface scattering. Figure 13b shows a  $K_a$  band Doppler spectrum calculated from the FFT of the I and Q signals at  $59^\circ$  V-pol, for a  $u_*$  of 8  $\text{cm s}^{-1}$ . The Doppler peak falls at about 76.7 Hz, which is about 6.3 Hz higher than Bragg theory predicts, from the intrinsic frequency and the drift velocity. The discrepancies between measured and predicted Bragg peaks are within the calibration error of  $u_*$ . While both Doppler spectra agree well with Bragg theory, only the corresponding  $K_a$  band  $\sigma_0$  agrees well with the composite surface predictions. All the X band data have been previously compared with scatterometer model function

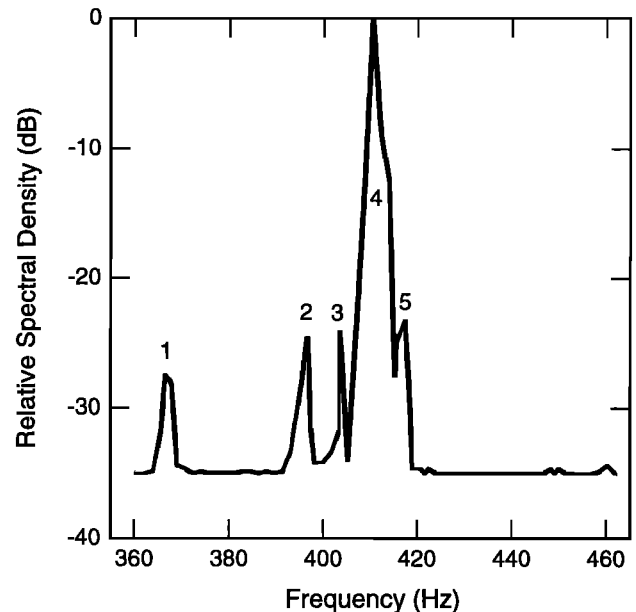
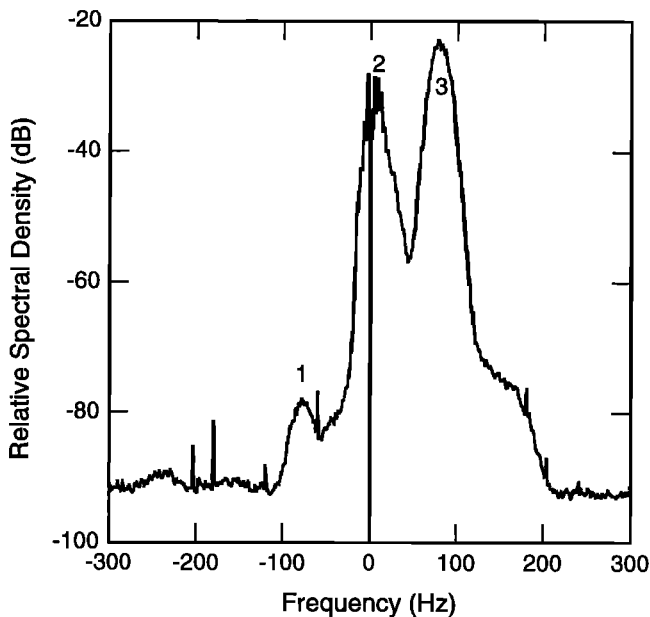


Figure 13a. Microwave Doppler spectrum at X band  $28^\circ$  V-pol. Peaks 1 and 5 are power line harmonics, peak 3 is the 403.5 Hz carrier frequency imbalance, or, effectively, zero Doppler shift, peak 4 is the Bragg peak for the downwind traveling Bragg waves, and peak 2 is the Bragg peak for the upwind traveling Bragg waves. Peak 4 is 8.75 Hz away from the carrier imbalance, which, for  $u_*$  of 15  $\text{cm s}^{-1}$ , is predicted by Bragg theory at 9.07 Hz. Peak 2 is 8.13 Hz away from the carrier imbalance.



**Figure 13b.** Microwave Doppler spectrum at  $K_a$  band  $59^\circ$  V-pol. Peak 2 represents IF system noise. Peaks 1 and 3 are at about  $\pm 76.7$  Hz, which, for  $u_*$  of  $8 \text{ cm s}^{-1}$ , is predicted by Bragg theory at  $70.4$  Hz.

predictions [see Keller *et al.*, 1992] without any special discrepancy being observed in any  $u_*$  regions. We note that correlations between the short wave spectral density and the long wave slope have not been taken into account in the composite surface theories used here. Plant [1986] has calculated such effects to second order in long wave slope using a linear modulation transfer function and found them to be 1 to 2 dB effects in general. This predicted level agreed rather well with studies of the azimuth angle dependence of  $\sigma_0$ . Thus, they probably do not explain the observed discrepancies.

## Discussion and Conclusions

We have measured two-dimensional spectra of upwind/downwind slopes of short wind-generated waves in a wave tank using a CCD optical system in conjunction with a light source with a known gradient below the tank. From these measured slope spectra, we have extracted the slope spectral density of waves traveling in the upwind/downwind direction and, from them, wave height variance spectra of these waves. The spectral densities evaluated at the Bragg-resonant wavenumber were used in both pure Bragg scattering theory and composite surface scattering theory to predict the normalized microwave cross section for backscattering from the rough water surface. We were able to measure the mean squared long wave slope needed in the composite surface model directly from the optical measurements assuming a cutoff wavelength three times the Bragg wavelength. The resulting  $\sigma_0$  were compared with those measured at  $X$  and  $K_a$  bands by CW microwave systems observing the same spot as the optical system but at a different

time. The microwave systems always looked upwind and were operated at five different incidence angles between  $28^\circ$  and  $68^\circ$ .

We found that the predictions of composite surface theory were generally closer to the measured values of  $\sigma_0$  than were those of pure Bragg scattering theory. Except in the case of V-pol  $X$  band  $\sigma_0$  at  $68^\circ$  incidence angle, we found that the predicted values were below the measured values. We conclude from our measurements that composite surface theory cannot explain H-pol  $\sigma_0$  at large incidence angles. For incidence angles below about  $60^\circ$  and for V-pol backscatter up to about  $70^\circ$ , composite surface theory accounts for much of the observed  $u_*$  dependence of the data. The fact that it seems to underpredict most  $\sigma_0$  values, however, means that our data cannot rule out the possibility that other scattering mechanisms also contribute significantly to backscatter from wind-roughened water surfaces.

The information gathered from the microwave/optical comparison suggests several future avenues of research. First, the optical system should be useful in analyses of long wave-short wave interactions, such as calculating the hydrodynamic modulation transfer function (mtf). Second, since  $K_a$  band is explained by composite theory about as well as  $X$  band, a higher resolution optical system could be used to probe further into the millimeter-wave regime, where scattering must eventually transition to all specular. Third,  $\sigma_0$  statistics should be related, in some fashion, to the statistics of short waves. In future work, we hope to address some or all of these problems.

**Acknowledgments.** The authors would like to thank several technicians and programmers, without whom this work would truly have been impossible. Norm Pollack assembled the electronics and the cart to hold the LUDOX tank and optical system under the wave tank, as well as building the track system to keep the optical cart in place, and, with Peter Richardson, designed and constructed the new fixed range, variable incidence angle arch for the scatterometers. John Alexander was responsible for the construction of the microwave anechoic chamber, and assisted in the transfer of the scatterometers to the fixed range, variable incidence angle arch. Wah Eng constructed the  $K_a$  band scatterometer and assisted in the internal calibration. David S. Raley wrote the data acquisition program, DT2EXA, that was used to collect wind speed, wind stress, wave height,  $K_a$  band I&Q, and Doppler  $X$  band data. He also wrote demuxing data processing software, and converted the software for generating I and Q from the  $X$  band Doppler signal from IDL to C. David McGown drafted some of the figures and typeset the paper. We would also like to thank Mark Donelan, who made many helpful suggestions about an early draft of this paper. This research was supported by ONR Research Option 83-2570 and NRL basic research funds 83-1319, 42-1319, and 72-1319, and ONR grants N00014-89-J-3224 and N00014-93-I-0016.

## References

- Apel, J. R., An improved model of the ocean surface wave vector spectrum and its effects on radar backscatter, *J. Geophys. Res.* 99, 16,269-16,291, 1994.

- Banner, M. L., I. S. F. Jones, and J. C. Trinder, Wavenumber spectra of short gravity waves, *J. Fluid Mech.*, 198, 321-344, 1989.
- Bass, F. G., I. M. Fuks, A. I. Kalmykov, I. E. Ostrovsky, and A. D. Rosenberg, Very high frequency radiowave scattering by a disturbed sea surface, 1, Scattering from a slightly disturbed boundary, *IEEE Trans. Antennas Propag.*, AP-16, 554-559, 1968a.
- Bass, F. G., I. M. Fuks, A. I. Kalmykov, I. E. Ostrovsky, and A. D. Rosenberg, Very high frequency radiowave scattering by a disturbed sea surface, 2, Scattering from a actual sea surface, *IEEE Trans. Antennas Propag.*, AP-16, 560-568, 1968b.
- Cox, C. S., Measurements of slopes of high-frequency wind waves, *J. Mar. Res.*, 16, 199-225, 1958.
- Cox, C. S., and W. H. Munk, Statistics of the sea surface derived from sun glitter, *J. Mar. Res.*, 13, 198-227, 1954.
- Donelan, M. A., and W. J. Pierson, Radar scattering and equilibrium ranges in wind-generated waves with application to scatterometry, *J. Geophys. Res.*, 92, 4971-5029, 1987.
- Durden, S. L., and J. F. Vesecky, A physical radar cross-section model for a wind-driven sea with swell, *IEEE J. Oceanic Eng.*, OE-10, 445-451, 1985.
- Ebuchi, N., H. Kawamura, and Y. Toba, Fine structure of laboratory wind-wave surfaces studied using an optical method, *Boundary Layer Meteorol.*, 39, 133-151, 1987.
- Gotwols, B. L., and W. C. Keller, Radar backscatter statistics from water waves, in OCEANS '90, Engineering in the Ocean Environment, *IEEE Publ. 90CH2858-9*, pp. 240-242, Inst. of Elec. and Electron. Eng., New York, 1990.
- Grant, C. R., and B. S. Yaplee, Back scattering from water and land at centimeter and millimeter wavelengths, *Proc. IRE*, 45, 976-982, 1957.
- Holliday, D., Resolution of a controversy surrounding the Kirchoff approach and the small perturbation method in rough scattering theory, *IEEE Trans. Antennas Propag.*, AP-35, 120-122, 1987.
- Jähne, B., Energy balance in small-scale waves - an experimental approach using optical slope measuring technique and image processing, in *Radar Scattering from Modulated Wind Waves*, edited by G. J. Komen and W. A. Oost, pp. 105-120, Kluwer Academic, Norwell, Mass., 1989.
- Jähne, B., and K. S. Riemer, Two-dimensional wave number spectra of small-scale water surface waves, *J. Geophys. Res.*, 95, 11531-11546, 1990.
- Jähne, B., and H. Schultz, Calibration and accuracy of optical slope measurements for short wind waves, *SPIE Int. Soc. Opt. Eng.*, vol. 1749, pp. 222-233, 1992.
- Jähne, B., S. Waas, and J. Klinke, A critical review of optical techniques for short ocean wave measurements, *SPIE Int. Soc. Opt. Eng.*, vol. 1749, pp. 204-215, 1992.
- Keller, M. R., W. C. Keller, and W. J. Plant, A wave tank study of the dependence of  $X$  band cross-sections on wind speed and water temperature, *J. Geophys. Res.*, 97, 5771-5792, 1992.
- Keller, W. C., and B. L. Gotwols, Two-dimensional optical measurement of wave slope, *Appl. Opt.* 22, 3476-3478, 1983.
- Kitaigorodskii, S. A., On the theory of the equilibrium range in the spectrum of wind-generated gravity waves, *J. Phys. Oceanogr.*, 13, 816-827, 1983.
- Klinke, J., and B. Jähne, 2D wave number spectra of short wind waves - results from wind wave facilities and extrapolation to the ocean, *SPIE Int. Soc. Opt. Eng.*, vol. 1749, pp. 245-257, 1992.
- Masuko, H., K. Okamoto, M. Shimada, and S. Niwa, Measurements of microwave backscattering signatures of the ocean surface using  $X$  band and  $K_a$  band airborne scatterometers, *J. Geophys. Res.*, 91, 13,065-13,083, 1986.
- Phillips, O. M., The equilibrium range in the spectrum of wind-generated ocean waves, *J. Fluid Mech.*, 4, 426-434, 1958.
- Phillips, O. M., Spectral and statistical properties of the equilibrium range in wind-generated gravity waves, *J. Fluid Mech.*, 156, 505-531, 1985.
- Plant, W. J., A two-scale model of short wind-generated waves and scatterometry, *J. Geophys. Res.*, 91, 10,735-10,749, 1986. (Correction, *J. Geophys. Res.*, 93, 1347, 1988.)
- Plant, W. J., Bragg scattering of electromagnetic waves from the air/sea interface, in *Surface Waves and Fluxes*, vol 2, edited by G. L. Geernaert and W. J. Plant, pp. 41-108, Kluwer Academic, Norwell, Mass., 1990.
- Plant, W. J., and W. C. Keller, Evidence of Bragg scattering in microwave Doppler spectra of sea return, *J. Geophys. Res.*, 95, 16,299-16,310, 1990.
- Plant, W. J., and J. W. Wright, Phase speeds of upwind and downwind traveling short gravity waves, *J. Geophys. Res.*, 85, 3304-3310, 1980.
- Rice, S. O., Reflection of electromagnetic waves from slightly rough surfaces, *Commun. Pure Appl. Math.*, 4, 351-379, 1951.
- Thompson, D. R., Doppler spectra from the ocean surface with a time-dependent composite model, in *Radar Scattering from Modulated Wind Waves*, edited by G. J. Komen and W. A. Oost, pp. 27-40, Kluwer Academic, Norwell, Mass., 1989.
- Thompson, D. R., B. L. Gotwols, and W. C. Keller, A comparison of  $K_u$  band Doppler measurements at  $20^\circ$  incidence with predictions from a time-dependent scattering model, *J. Geophys. Res.*, 96, 4947-4955, 1991.
- Valenzuela, G. R., Theories for the interaction of electromagnetic and oceanic waves-A review, *Boundary Layer Meteorol.*, 13, 61-85, 1978.
- van Halsema, D., C. Calkoen, W. A. Oost, P. Snoeij, J. Vogelzang, and B. Jähne, Comparisons of backscattering calculations with measurements made in a large wind/wave flume, in IGARSS '92, International Space Year: Space Remote Sensing, *IEEE Publ. 92CH3041-2*, pp. 1451-1453, Inst. of Elec. and Electron. Eng., New York, 1992.
- Waas, S., and B. Jähne, Combined slope-height measurements of short wind waves: first results from field and laboratory measurements, *SPIE Int. Soc. Opt. Eng.*, vol. 1749, pp. 295-306, 1992.
- Witting, J. M., and J. W. Wright, Microwave scattering and the dynamics of short wind waves, *Rep. NRL Prog.*, 1-16, February 1975.
- Wright, J. W., Backscattering from capillary waves with application to sea clutter, *IEEE Trans. Antennas Propag.*, AP-14, 749-754, 1966.
- Wright, J. W., A new model for sea clutter, *IEEE Trans. Antennas Propag.*, AP-16, 217-223, 1968.
- Wright, J. W., and W. C. Keller, Doppler spectra in microwave scattering from wind waves, *Phys. Fluids*, 14, (3), 466-474, 1971.

B. L. Gotwols, Applied Physics Laboratory, Johns Hopkins University, Laurel, MD 20723

M. R. Keller, Naval Research Laboratory, Washington, DC 20375

W. C. Keller and W. J. Plant, Applied Physics Laboratory, University of Washington, Seattle, WA 98105

(Received June 23, 1994; revised February 24, 1995; accepted February 24, 1995.)